CORA Cork Open Research Archive
Cartlann Taighde Oscailte Chorcaí

Title	Impact of disorder on the optoelectronic properties of GaNyAs1–x–yBix alloys and heterostructures
Authors	Usman, Muhammad;Broderick, Christopher A.;O'Reilly, Eoin P.
Publication date	2018-10-09
Original Citation	Usman, M., Broderick, C. A. and O'Reilly, E. P. (2018) 'Impact of disorder on the optoelectronic properties of GaNyAs1–x–yBix alloys and heterostructures', Physical Review Applied, 10(4), 44024 (17pp). doi:10.1103/PhysRevApplied.10.044024
Type of publication	Article (peer-reviewed)
Link to publisher's version	https://link.aps.org/doi/10.1103/PhysRevApplied.10.044024 - 10.1103/PhysRevApplied.10.044024
Rights	© 2018 American Physical Society. All rights reserved.
Download date	2026-11-01 07:06:13
Item downloaded from	https://hdl.handle.net/10468/7297

UCC
University College Cork, Ireland
Coláiste na hOllscoile Corcaigh

Impact of Disorder on the Optoelectronic Properties of $GaN_yAs_{1-x-y}Bi_x$ Alloys and Heterostructures

Muhammad Usman,[1,*] Christopher A. Broderick,[2,3] and Eoin P. O'Reilly[2,4]

[1] *School of Physics, University of Melbourne, Parkville, Melbourne, Victoria 3010, Australia*
[2] *Tyndall National Institute, Lee Maltings, Dyke Parade, Cork T12 R5CP, Ireland*
[3] *Department of Electrical and Electronic Engineering, University of Bristol, Bristol BS8 1UB United Kingdom*
[4] *Department of Physics, University College Cork, Cork T12 YN60, Ireland*

(Received 12 January 2018; revised manuscript received 20 June 2018; published 9 October 2018)

We perform a systematic theoretical analysis of the nature and importance of alloy disorder effects on the electronic and optical properties of $GaN_yAs_{1-x-y}Bi_x$ alloys and quantum wells (QWs), using large-scale atomistic supercell electronic structure calculations based on the tight-binding method. Using ordered alloy supercell calculations, we also derive and parametrize an extended-basis 14-band $\mathbf{k}\cdot\mathbf{p}$ Hamiltonian for $GaN_yAs_{1-x-y}Bi_x$. Comparison of the results of these models highlights the role played by short-range alloy disorder—associated with substitutional nitrogen (N) and bismuth (Bi) incorporation—in determining the details of the electronic and optical properties. Systematic analysis of large alloy supercells reveals that the respective impacts of N and Bi on the band structure remain largely independent, a robust conclusion that we find to be valid even in the presence of significant alloy disorder where N and Bi atoms share common Ga nearest neighbors. Our calculations reveal that N- (Bi-)related alloy disorder strongly influences the conduction- (valence-)band edge states, leading in QWs to strong carrier localization, as well as inhomogeneous broadening and modification of the conventional selection rules for optical transitions. Our analysis provides detailed insight into key properties and trends in this unusual material system, and enables quantitative evaluation of the potential of $GaN_yAs_{1-x-y}Bi_x$ alloys for applications in photonic and photovoltaic devices.

DOI: 10.1103/PhysRevApplied.10.044024

I. INTRODUCTION

Over the past several decades, significant research effort has been dedicated to the development of III-V semiconductor alloys and quantum-confined heterostructures such as quantum wells [1–6] and quantum dots [7–13], as platforms for the development of a range of photonic, photovoltaic, and spintronic devices. Despite the widespread use of InP-based quantum-well- (QW-)based devices in optical communications, an important factor limiting overall device performance is the prevalence of temperature-dependent loss mechanisms, including carrier leakage, as well as nonradiative Auger recombination and intervalence band absorption (IVBA) processes involving transitions between the highest-energy valence bands (VBs) and the spin split-off (SO) band [14–16]. As these loss mechanisms are governed by the fundamental parameters of the material band structure—in particular, the band gap (E_g) and the VB spin-orbit splitting energy (Δ_{SO})—any attempt to mitigate them must focus on developing materials and heterostructures the electronic properties of which can be flexibly engineered [17–19].

Recently, dilute bismide alloys have emerged as a promising new material system the band structure of which can be engineered in order to suppress IVBA and Auger recombination [18,20]. Dilute bismides are formed when a dilute fraction of Bi atoms replace As in (In)GaAs, forming the $(In)GaAs_{1-x}Bi_x$ alloy. The incorporation of Bi leads to an extremely strong reduction and composition-dependent bowing of E_g, of approximately 90 meV between $x = 0$ and 1% in $GaAs_{1-x}Bi_x$. Contrary to N incorporation in GaAs, which strongly perturbs the conduction-band (CB) structure, leading to a reduction of E_g of approximately 150 meV between $y = 0$ and 1% in GaN_yAs_{1-y} [21–23], Bi—being significantly larger and more electropositive than As or N—primarily impacts the VB [24–27]. As a result, the strong reduction of E_g in $GaAs_{1-x}Bi_x$ is accompanied by a similarly large increase and bowing of Δ_{SO} [27–29]. This brings about the potential to engineer the band structure to achieve $\Delta_{SO} > E_g$ and hence to facilitate suppression of the dominant Auger recombination and IVBA mechanisms [18,30,31]. Given the strong and complementary nature of the impact of N and Bi incorporation

*musman@unimelb.edu.au

 © 2018 American Physical Society

on the GaAs band structure, coalloying to form the quaternary dilute nitride-bismide alloy $GaN_yAs_{1-x-y}Bi_x$ provides significant opportunities for band-structure engineering [18,24,30,32]. N (Bi) incorporation primarily impacts the CB (VB) structure and introduces tensile (compressive) strain with respect to a GaAs substrate, suggesting that the band gap, VB structure, band offsets, and strain can all be readily engineered. Initial experimental studies [33–36] have revealed the expected giant reduction and bowing of E_g, confirming that $GaN_yAs_{1-x-y}Bi_x$ alloys offer an interesting platform from the perspective of photonic and photovoltaic device development.

To fully exploit the novel characteristics of $GaN_yAs_{1-x-y}Bi_x$, a comprehensive theoretical understanding of the properties of this emerging semiconductor alloy must be developed. Given the highly mismatched nature of N- and Bi-containing semiconductor alloys—in which substitutional N and Bi atoms act as isovalent impurities, generating localized states that hybridize with the extended (Bloch) states of the host-matrix semiconductor, leading to a breakdown in Bloch character—conventional theoretical approaches to modeling alloy band structure, such as the virtual-crystal (VC) approximation, break down (as is the case, to a lesser extent, even in more conventional semiconductor alloys [37]). These unusual material properties then mandate that a direct atomistic approach, free of limiting approximations, is necessary to understand the strongly perturbed electronic structure [22,23,25,27,38]. In particular, based on previous investigations [39,40] of GaN_yAs_{1-y} and $GaAs_{1-x}Bi_x$ alloys, it is expected that short-range alloy disorder—associated with the formation of pairs and larger clusters of N and/or Bi atoms sharing common Ga nearest neighbors—will have a pronounced effect on $GaN_yAs_{1-x-y}Bi_x$ alloy properties. Previous studies have been primarily based on continuum approaches, which typically ignore disorder effects and therefore offer limited scope to understand the full details of the complicated alloy electronic structure or to analyze the results of experimental measurements [30,41,42]. Here, we present a multiscale framework based on atomistic tight-binding (TB) and continuum **k·p** models to describe the electronic and optical properties of $GaN_yAs_{1-x-y}Bi_x$ alloys and heterostructures. Through systematic large-scale atomistic TB calculations, we develop a detailed understanding of $GaN_yAs_{1-x-y}Bi_x$ alloys and QW structures; in particular, highlighting the crucial significance of alloy disorder effects and the associated implications for the interpretation of future experimental measurements and for the development of heterostructures for device applications.

We begin our analysis by undertaking large-scale electronic structure calculations on ordered alloy supercells and quantify the impact of coalloying N and Bi on the GaAs electronic structure in the ultradilute (dilute-doping) limit. Our results show that N and Bi effectively perturb the electronic properties independently of one another. For large, disordered alloy supercells, we compute the evolution of the electronic structure with alloy composition, revealing general trends and demonstrating, somewhat surprisingly, that the respective impact of N and Bi incorporation on the electronic properties remains independent, even in the presence of significant short-range alloy disorder. Our analysis demonstrates that an extended-basis-set 14-band **k·p** Hamiltonian—which explicitly treats the localized impurity states associated with substitutional N and Bi atoms, and is parametrized directly via atomistic supercell calculations—describes the main features of the band-structure evolution with reasonable accuracy compared both to full atomistic calculations and experimental measurements. We perform atomistic and continuum calculations of the electronic and optical properties of $GaN_yAs_{1-x-y}Bi_x$/GaAs QWs, the results of which highlight the role played by alloy disorder in determining the properties of technologically relevant heterostructures. On the basis of our analysis, we then evaluate the potential to develop devices for practical applications: (i) we suggest, contrary to recent studies [43–45], that $GaN_yAs_{1-x-y}Bi_x$ heterostructures are not suitable for applications at 1.55 μm; and (ii) we confirm that the most promising potential application of $GaN_yAs_{1-x-y}Bi_x$ alloys is as an approximately 1 eV band-gap material, grown lattice-matched to GaAs (or Ge) for applications in multijunction solar cells [46]. Overall, our results elucidate the unusual properties of $GaN_yAs_{1-x-y}Bi_x$, highlight the importance of short-range alloy disorder in determining the details of the material properties and provide guidelines for the development of optimized photonic and photovoltaic devices based on this emerging semiconductor alloy.

The remainder of this paper is organized as follows. In Sec. II, we describe our atomistic TB and continuum **k·p** models of the $GaN_yAs_{1-x-y}Bi_x$ electronic structure. Next, in Sec. III, we present our results, beginning in Sec. III A with an analysis of the impact of coalloying N and Bi on the electronic properties in the dilute-doping limit, before turning in Sec. III B to analyze the evolution of the electronic structure in disordered alloys and then the respective electronic and optical properties of $GaN_yAs_{1-x-y}Bi_x$/GaAs QWs in Secs. III C and III D. In Sec. IV, we describe the implications of the calculated trends in the electronic and optical properties for practical applications. Finally, we summarize and conclude in Sec. V.

II. THEORETICAL MODELS

The unusual electronic properties of dilute nitride and bismide alloys derive from the fact that, when incorporated in dilute concentrations, N and Bi act as isovalent impurities that strongly perturb the band structure of the host-matrix semiconductor. Due to the prominence of N-

and Bi-related impurity effects, conventional approaches to analyzing alloy band structures—e.g., the VC approximation—break down, meaning that direct atomistic calculations are generally required to provide quantitative insight [23,47,48]. Furthermore, since the effects of Bi and N incorporation are prominent at dilute compositions, quantitative understanding of the properties of real materials must be built on analysis of systems containing upwards of thousands of atoms, in order to mitigate finite-size effects and so that there is sufficient scope to analyze important alloy disorder effects [27,49].

Here, we provide an overview of the atomistic TB and continuum **k·p** models we have developed to study the $GaN_yAs_{1-x-y}Bi_x$ electronic structure. Full details of these models, including the parameters used in our calculations, can be found in Sec. 1 of the Supplemental Material [50].

A. Atomistic: sp^3s^* tight-binding model

Since the TB method employs a basis of localized atomic orbitals, it is ideally suited to probe the electronic structure of localized impurities [51]. This, combined with its low computational cost compared to first-principles methods, means that appropriately parametrized TB models provide a physically transparent and highly effective means by which to systematically analyze the properties of large disordered systems and realistically sized heterostructures. We have previously demonstrated that the TB method provides a detailed understanding of the electronic and optical properties of GaN_yAs_{1-y} and $GaAs_{1-x}Bi_x$ alloys and that calculations based on this approach are in quantitative agreement with a wide range of experimental data [23,27,49,52,53]. Here, we extend this approach to $GaN_yAs_{1-x-y}Bi_x$ alloys.

Our nearest-neighbor sp^3s^* TB model for $GaN_yAs_{1-x-y}Bi_x$ is closely based upon that developed in Ref. [27] for dilute bismide alloys, which we have previously employed to provide quantitative understanding of the electronic [27], optical [49], and spin [53] properties of $GaAs_{1-x}Bi_x$. In this model, which explicitly includes the effects of spin-orbit coupling, the orbital energies at a given atomic site are computed depending explicitly on the local neighbor environment: the interatomic interactions are taken to vary with the relaxed nearest-neighbor (i) bond lengths via a generalization of Harrison's scaling rule [54,55] and (ii) bond angles via the two-center expressions of Slater and Koster [56]. To treat $GaN_yAs_{1-x-y}Bi_x$, we have made one significant modification to this model, by including an on-site renormalization that corrects the orbital energies at a given atomic site depending on the local displacement of the atomic positions due to lattice relaxation. This simple modification—which depends only on the differences in atomic orbital energies and bond lengths between the constituent GaN, GaAs, and GaBi compounds—is motivated by our previous analysis of GaN_yAs_{1-y} alloys, where we found that it suitably describes the charge transfer associated with the nonlocal character of the change in the supercell Hamiltonian due to substitutional N incorporation [54]. As in Ref. [27], the relaxed atomic positions in the alloy supercells are computed using a valence force field model based on the Keating potential [58,59]. We note that this TB-based approach reproduces the detailed features of the electronic structure of N- and Bi-containing alloys compared to first-principles calculations based on density-functional theory. A detailed description of our theoretical framework can be found in our recently published review of the theory and simulation of dilute bismide alloys [40], where the validity of this approach is evaluated in the context of first-principles calculations and experimental measurements.

To study the properties of bulk $GaN_yAs_{1-x-y}Bi_x$ alloys, we employ simple-cubic supercells containing 4096 atoms. We have previously demonstrated that this supercell size is sufficiently large to (i) mitigate finite-size effects on the calculated electronic properties, by providing a suitably large basis of folded bulk states with which to describe N- and Bi-related localized states, and (ii) provide sufficient scope for the formation of a large variety of distinct local atomic environments to accurately reflect the short-range alloy disorder inherent in real materials. Our heterostructure calculations are performed for realistically sized [001]-oriented $GaN_yAs_{1-x-y}Bi_x$/GaAs QWs. The 24 576-atom supercells used to study these structures have a total length of 24 nm along the [001] direction and 4 nm along each of the [100] and [010] in-plane directions. The thickness of the $GaN_yAs_{1-x-y}Bi_x$ QW layer is taken to be 8 nm in each case, with surrounding 8 nm thick GaAs barrier layers. The lateral extent and thickness of these QWs are chosen based on our analysis of $GaAs_{1-x}Bi_x$/GaAs QWs [60,61], where we note that (i) the lateral dimensions are sufficient to mitigate in-plane finite-size effects and (ii) the calculated properties are robust to QW thickness fluctuations of approximately ± 1 nm. All bulk and QW supercell calculations employ conventional Born–von Karman boundary conditions. In order to analyze the optical properties, we compute the transverse electric (TE-) and transverse magnetic (TM-)polarized—i.e., polarized perpendicular or parallel to [001]—optical transition strengths in the usual way, by using Fermi's "golden rule" in conjunction with the full supercell eigenstates **(**cf., Eq. (4) in the Supplemental Material [50]**)**.

B. Continuum: 14-band k·p Hamiltonian

Previous analysis has demonstrated that it is useful to derive continuum models that describe the perturbed band structure of GaN_yAs_{1-y} and $GaAs_{1-x}Bi_x$ alloys. Phenomenological approaches, principally the band-anticrossing (BAC) model, have originated from

interpretation of spectroscopic data [21,62] and atomistic electronic structure calculations [42,63,64] and are widely employed as a straightforward means by which to describe the evolution with alloy composition of the main features of the band structure of bulk materials and heterostructures. For GaN_yAs_{1-y}, it is well established that the CB structure can be described by a simple two-band BAC model, in which the extended states of the GaAs host-matrix CB edge interact with a set of higher-energy N-related localized states [21,23]. In $Ga(In)N_yAs_{1-y}$, the composition dependence of the BAC interaction between these two sets of states results in a strong reduction of the alloy CB-edge energy with increasing y. Similar behavior is present in $GaAs_{1-x}Bi_x$: the strong reduction (increase) and composition-dependent bowing of E_g (Δ_{SO}) can be described in terms of a valence band–anticrossing (VBAC) interaction [42,62] between the extended states of the GaAs VB edge and localized impurity states associated with substitutional Bi impurities, which pushes the alloy VB edge upward in energy with increasing x. While (V)BAC models generally omit effects associated with alloy disorder, they nonetheless provide reliable descriptions of the main features of the alloy band structure [42,65,66] and have been used as a basis to provide quantitative prediction of the properties of real dilute nitride and bismide photonic and photovoltaic devices [67,68].

We have previously demonstrated that an appropriate set of $\mathbf{k}\cdot\mathbf{p}$ basis states for $GaN_yAs_{1-x-y}Bi_x$ alloys must represent a minimum of 14 bands: the spin-degenerate CB, light-hole (LH), heavy-hole (HH), and SO bands of the GaAs host matrix (eight bands), the A_1-symmetric N localized states (of which there is one spin-degenerate set; two bands), and the T_2-symmetric Bi localized states (of which there are two spin-degenerate sets; four bands). Atomistic supercell calculations confirm that the respective impacts of N and Bi on the band structure are decoupled in ordered $GaN_yAs_{1-x-y}Bi_x$ alloys, confirming that an appropriate $\mathbf{k}\cdot\mathbf{p}$ Hamiltonian can be constructed by directly superposing the separate VC, (V)BAC, and strain-dependent contributions associated with N and Bi incorporation [42]. As such, the $GaN_yAs_{1-x-y}Bi_x$ band structure then admits a simple interpretation in terms of the respective perturbation of the CB and VB separately by N- and Bi-related localized states, with minor VC changes to the CB (VB) structure due to Bi (N) incorporation. We parametrize the 14-band $\mathbf{k}\cdot\mathbf{p}$ Hamiltonian directly from TB supercell calculations, obtaining the N- and Bi-related band parameters without the usual requirement to perform *post hoc* fitting to the results of alloy experimental data [42,63].

III. RESULTS AND DISCUSSIONS

A. Coalloying N and Bi: the dilute-doping limit

Analysis of large ordered $2M$-atom $Ga_MN_1As_{M-1}$ and $Ga_MAs_{M-1}Bi_1$ supercells—undertaken using the empirical pseudopotential [22,47,69] and TB methods [27,42,63,70]—has revealed the mechanisms by which substitutional N and Bi impurities perturb the GaAs band structure. Specifically, it has been shown that the local relaxation of the crystal lattice (arising from differences in covalent radius) and charge transfer (arising from differences in atomic orbital energies) due to substitutional incorporation of an isolated N (Bi) impurity gives rise to highly localized states. These states are resonant with and couple to the GaAs CB (VB) in GaN_yAs_{1-y} ($GaBi_xAs_{1-x}$), leading to hybridized alloy CB (VB) edge states containing an admixture of extended GaAs Bloch and localized N (Bi) character. These localized states can be described as linear combinations of the supercell eigenstates that fold back to Γ. Since more eigenstates fold back to Γ with increasing supercell size, systematic analysis has demonstrated the need to use large supercells—i.e., ultradilute Bi and N compositions—to accurately quantify the nature and impact of these localized impurity states in the dilute-doping limit [27,42,63,71].

Here, we perform a similar analysis for a series of 4096-atom $Ga_{2048}N_1As_{2046}Bi_1$ supercells. We vary the relative positions of the N and Bi atoms to ascertain (i) any changes to their respective impact on the electronic structure and (ii) the scale of any interactions between N- and Bi-related localized states. In each case, we compute the fractional GaAs Γ (Bloch) character [48,49] of the supercell zone-center eigenstates in order to quantify the changes in the electronic structure associated with the formation of different N and Bi local atomic environments. Full details of the calculated Γ character spectra are presented in Sec. 2 of the Supplemental Material [50].

Table I summarizes the results of our calculations for a range of $Ga_{2048}N_1As_{2046}Bi_1$ supercells. We use subscripts B, C, and D to describe the positions of Bi atoms relative to a N atom at position A. Prior to relaxation of the atomic positions, the vectors describing the separation between these atomic sites are $\mathbf{r}_{AB} = a_0(\hat{x}+\hat{y}+\hat{z})$, $\mathbf{r}_{AC} = a_0(\hat{x}+\hat{y})$ and $\mathbf{r}_{AD} = \frac{a_0}{2}(\hat{x}+\hat{y})$, where a_0 is the GaAs lattice constant. For example, the notation $GaAs{:}N_ABi_B$ describes a supercell in which the Bi atom is oriented along [111] relative to the N atom, with the N and Bi atoms occupying the same position in a given pair of neighboring eight-atom simple-cubic unit cells, while the notation $GaAs{:}N_ABi_D$ describes a [110] oriented N-Ga-Bi complex in which the N and Bi atoms share a common Ga nearest neighbor.

We begin with a $Ga_{2048}N_1As_{2046}Bi_1$ supercell in which the N and Bi atoms are separated by $\sqrt{3}a_0$ (where they do not form a pair or cluster) and note that the associated reduction in symmetry, arising from relaxation of the crystal lattice about the impurity sites, lifts the degeneracy of the predominantly GaAs LH- and HH-like VB edge states. As the N and Bi atoms are brought closer together, the splitting between these states increases due to the resultant larger local relaxation of the lattice, with

TABLE I. The energies of the lowest-energy CB (E_{CB}), two highest-energy VBs ($E_{VB,1}$ and $E_{VB,1}$), and the SO-band edge (E_{SO}) calculated using the TB method for selected 4096-atom simple-cubic $GaN_yAs_{1-x-y}Bi_x$ supercells. The notation describing distinct (nonequivalent) local atomic configurations in the second column is defined in the text; accompanying schematic illustrations can be found in Fig. 1 of the Supplemental Material [50]. The spatial distance between the N and Bi atoms for each (unrelaxed) configuration is denoted by $r_{N,Bi}$ and given in units of the GaAs lattice constant a_0.

Supercell	Configuration	$r_{N,Bi}$ (a_0)	E_{CB} (eV)	E_{V1} (eV)	E_{V2} (eV)	E_{SO} (eV)
$Ga_{2048}As_{2048}$	GaAs	—	1.519	0.0010	0.0010	−0.3518
$Ga_{2048}N_1As_{2047}$	GaAs : N_A	—	1.500	0.0013	0.0011	−0.3518
$Ga_{2048}As_{2047}Bi_1$	GaAs : Bi_B	—	1.518	0.0068	0.0062	−0.3521
$Ga_{2048}N_1As_{2046}Bi_1$	GaAs : N_ABi_B	$\sqrt{3}$	1.500	0.0152	0.0131	−0.3521
$Ga_{2048}N_1As_{2046}Bi_1$	GaAs : N_ABi_C	$\sqrt{2}$	1.506	0.0154	0.0127	−0.3521
$Ga_{2048}N_1As_{2046}Bi_1$	GaAs : N_ABi_D	$\frac{1}{\sqrt{2}}$	1.495	0.0196	0.0115	−0.3523

the largest calculated splitting of approximately 10 meV in a $Ga_{2048}N_1As_{2046}Bi_1$ supercell occurring for an N-Ga-Bi complex oriented along the [110] direction (in which the N and Bi atoms are second-nearest neighbors and share a Ga nearest neighbor). We note that this lifting of the VB-edge degeneracy due to a reduction in symmetry is consistent with that calculated previously for disordered $GaAs_{1-x}Bi_x$ [27,49,72]. In the $Ga_{2048}N_1As_{2047}$ and $Ga_{2048}As_{2047}Bi_1$ supercells, we note the presence of a small (< 1 meV) splitting of the LH- and HH-like VB edge states. We do not expect a lifting of the VB-edge degeneracy in these ordered structures: the observed splitting is due to small residual strains associated with the convergence of the relaxation of the atomic positions using the valence force field model [27,49].

From Table I, we see that as the N and Bi atoms are brought closer together, the splitting between the two highest-energy VB states (E_{v1} and E_{v2}) increases due to the resultant larger local relaxation of the lattice. The largest calculated splitting of approximately 10 meV in a $Ga_{2048}N_1As_{2046}Bi_1$ supercell occurs when the N and Bi atoms are second-nearest neighbors sharing a Ga nearest neighbor (in the GaAs:N_ABi_D supercell). We note that this lifting of the VB-edge degeneracy due to a reduction in symmetry is consistent with that calculated previously for disordered $GaAs_{1-x}Bi_x$ [27,49,72]. We note also that the calculated shift in the VB-edge energy in the supercells containing both N and Bi is significantly larger than that in the equivalent N-free supercells. Our analysis suggests that this is a result of the large local relaxation of the lattice about the N atomic site which, within the framework of our TB model, generates significant shifts in the energies of the p orbitals localized on the N atom. However, we calculate that this trend does not persist beyond the ultradilute regime, with the calculated overall shift in the VB-edge energy with composition in $GaN_yAs_{1-x-y}Bi_x$ closely tracking that in $GaAs_{1-x}Bi_x$ (cf., Sec. III B).

The calculated trends in the impact of interaction between N- and Bi-related localized states is consistent with previous calculations [42] and can be understood generally on the basis of their respective independent impacts in $Ga_{2048}N_1As_{2047}$ and $Ga_{2048}As_{2047}Bi_1$ supercells. For the CB edge state, having energy E_{CB}, the impact of the interaction between the N and Bi atoms is minimal: the overall character of the CB edge is predominantly determined by the impact of the localized resonant state associated with the N atom. Even in the GaAs:N_ABi_B supercell—in which the N and Bi atoms are closest and hence the interaction of their associated localized states is maximized—the largest calculated Bi-induced shift in E_{CB} is minimal when compared to the overall shift in E_{CB} calculated in an equivalent Bi-free supercell. In this case, the character of the calculated $GaN_yAs_{1-x-y}Bi_x$ CB edge state results from a combination of an N-induced hybridization and reduction in energy (described by the conventional two-band BAC model), in addition to small further changes associated with (i) the VC-like Bi-induced reduction in E_{CB} and (ii) the local compressive strain associated with lattice relaxation about the Bi atomic site. Contrary to the trends observed for the CB and VB edges, we note that the SO-band-edge energy is relatively unaffected by N incorporation: the calculated trends in the energy of the Γ character of the SO-band edge states are essentially identical to those in $GaAs_{1-x}Bi_x$, with the impact of N manifesting primarily via small energy shifts associated with local lattice relaxation.

Next, we turn our attention to the localized states associated with N and Bi, which we construct explicitly for each supercell [27,48,63]. Our analysis reveals a somewhat surprising feature: the overall nature and character of the N- (Bi-)related localized states are found to be effectively identical to those in an equivalent Bi-free $Ga_{2048}N_1As_{2047}$ (N-free $Ga_{2048}As_{2047}Bi_1$) supercell. In all cases, we find that the character of the band-edge eigenstates is largely retained: the CB- (VB-)edge eigenstates are a linear combination of the unperturbed GaAs CB- (VB-)edge and N- (Bi-)localized states, describable via the same 2- (4-)band (V)BAC model as in GaN_yAs_{1-y} ($GaAs_{1-x}Bi_x$) [27,63]. This confirms that the impact of N (Bi) on the CB (VB) structure is effectively independent of coalloying with Bi

(N) and, as we will see below, that general trends in the evolution of the $GaN_yAs_{1-x-y}Bi_x$ band structure can be described to a reasonable degree of accuracy by superposing the established description of impact of both N and Bi incorporation [42].

B. Band-edge energies in disordered alloys

Having analyzed the impact of coalloying N and Bi in the dilute-doping limit, we now turn our attention to the evolution of the electronic structure with alloy composition in disordered alloys. We restrict our attention to lattice-matched 4096-atom supercells in which the N and Bi compositions have been chosen to produce zero net macroscopic strain with respect to GaAs—i.e., we require $y = 0.58x$ so that the $GaN_yAs_{1-x-y}Bi_x$ lattice constant computed using Végard's law is equal to that of GaAs. At each alloy composition, we compute the electronic structure of five distinct supercells in which the N and Bi atoms are substituted at randomly chosen sites on the anion sublattice. To determine the composition dependence of the band-edge energies, we average over the results of these five distinct calculations at each composition. As a reference for the $GaN_yAs_{1-x-y}Bi_x$ calculations, we have performed the same analysis for equivalent Bi- (N-) free GaN_yAs_{1-y} ($GaAs_{1-x}Bi_x$) supercells. The results of these calculations are summarized in Figs. 1(a), 1(b), and 1(c) for GaN_yAs_{1-y}, $GaAs_{1-x}Bi_x$, and $GaN_yAs_{1-x-y}Bi_x$, respectively.

Beginning with GaN_yAs_{1-y}, the closed red circles in Fig. 1(a) show the calculated dependence of the CB- and VB-edge energies E_{CB} and E_{VB} on y. Our calculations reproduce the well-known trends for GaN_yAs_{1-y}. First, N incorporation causes a rapid decrease and large composition-dependent bowing of E_{CB}, with the calculated CB edge states consisting of an admixture of GaAs CB-edge Bloch and N localized-state character [63,74]. Second, the VB- and SO-edge energies are relatively unperturbed from those calculated in ordered alloy supercells and are well described via conventional VC energy shifts as $E_{VB}(y) = E_{VB}(0) + \kappa_N y$ and $E_{SO}(y) = E_{SO}(0) - \gamma_N y$, where $E_{VB}(0)$ and $E_{SO}(0)$ are the corresponding unperturbed GaAs band-edge energies [42]. Third, the band gap $E_g = E_{CB} - E_{VB}$ [depicted by closed green squares in Fig. 1(a)] is calculated to decrease by approximately 180 meV when 1% of the As atoms are replaced by N, in good agreement with a range of experimental measurements [23].

The closed red circles in Fig. 1(b) show the calculated dependence of E_{CB} and E_{VB} on x in $GaAs_{1-x}Bi_x$. Again, we recover the experimentally observed trends. Bi incorporation causes a rapid decrease of the band gap (closed green squares), which is characterized by strong composition-dependent bowing and is qualitatively similar to that in GaN_yAs_{1-y} but instead originates from strong upward bowing of E_{VB} [62]. The calculated VB-edge eigenstates consist of an admixture of GaAs VB Bloch and Bi localized-state character [27,42] and the calculated approximately 100 meV decrease in E_g in going from GaAs to $GaAs_{0.99}Bi_{0.01}$ is in good agreement with experimental measurements [27,29]. We note that our calculations correctly describe that the decrease of E_g due to N incorporation is larger than that associated with Bi incorporation at fixed composition, reflecting the larger differences in covalent radius and electronegativity between N and As than between As and Bi. We further find that E_{CB} and the SO-band-edge energy E_{SO} in $GaAs_{1-x}Bi_x$ are well described via conventional VC energy shifts as $E_{CB}(x) = E_{VB}(0) - \alpha_{Bi}x$ and $E_{SO}(x) = E_{SO}(0) - \gamma_{Bi}x$ [42]. The calculated VC parameters $\kappa_{N,Bi}$, $\alpha_{N,Bi}$ and $\gamma_{N,Bi}$ are given, along with the remainder of the parameters of the 14-band **k·p** model, in Sec. 1.B of the Supplemental Material [50].

The error bars in Figs. 1(a) and 1(b) denote the standard deviations of the corresponding energies, computed from the values of E_{CB}, E_{VB} and E_g calculated for each of the distinct supercells considered at fixed alloy composition. For GaN_yAs_{1-y}, we note that the calculated standard deviations for E_{CB} (and hence E_g) increase strongly with increasing y, from 6 meV at an ultradilute N composition of $y = 0.15\%$ to > 80 meV for $2\% \lesssim y \lesssim 3\%$. This reflects the fact that N-related alloy disorder has a strong impact on the GaN_yAs_{1-y} CB structure, with the different spatially random distributions of N atoms in the supercells considered leading to large differences in the computed CB-edge energy at fixed y. Conversely, we compute negligible standard deviations $\lesssim 3$ meV for E_{VB} across the range of y considered, reflecting the weak impact of N incorporation on the VB structure. We find that these trends are reversed in $GaAs_{1-x}Bi_x$ alloys, where we compute negligible standard deviations $\lesssim 3$ meV for E_{CB} at each Bi composition x, reflecting the fact that VC contributions dominate the CB- and SO-band-edge character. However, we compute larger standard deviations for E_{VB}, reflecting the important role played by Bi-related localized states and alloy disorder in determining the nature of the $GaAs_{1-x}Bi_x$ VB edge states. However, the maximum calculated value of 43 meV for the standard deviation of E_{VB} at $x = 1.95\%$ is approximately one half of that calculated for GaN_yAs_{1-y} at similar composition, indicating, as expected, that N-related alloy disorder perturbs the electronic structure more strongly.

Figure 1(c) summarizes the results of the disordered alloy supercell calculations for $GaN_yAs_{1-x-y}Bi_x$ lattice-matched to GaAs. The variation of E_{CB}, E_{VB}, and E_g is shown here as a function of the Bi composition x, for N compositions $y = 0.58x$. The calculated reduction of E_g—approximately 220 meV (400 meV) in a lattice-matched alloy having $x = 1\%$ ($y = 1\%$)—is significantly larger than that in either GaN_yAs_{1-y} or $GaAs_{1-x}Bi_x$. That

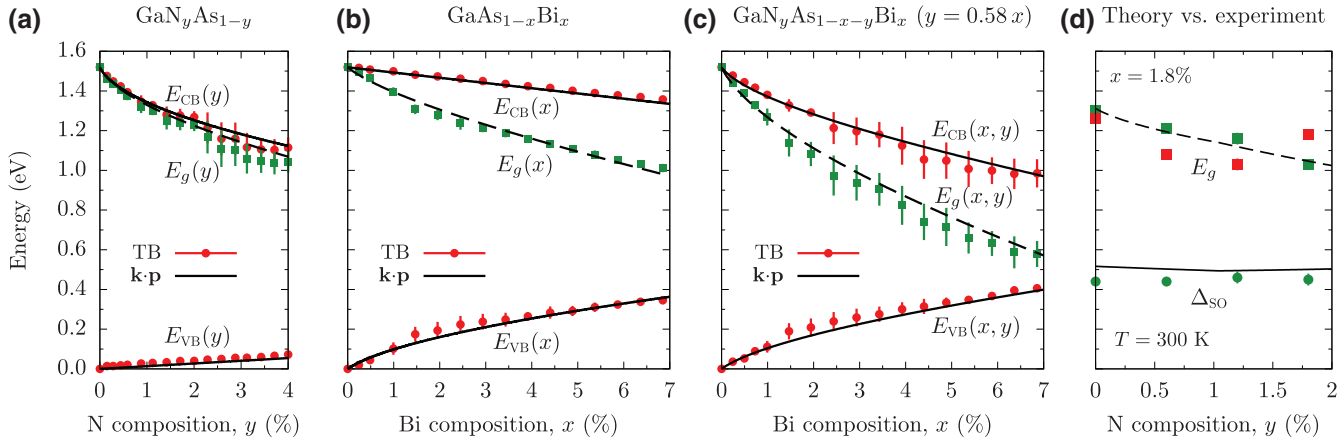


FIG. 1. (a)–(c) The calculated variation of the CB- and VB-edge energies E_{CB} and E_{VB}, and band gap $E_g = E_{CB} - E_{VB}$, with alloy composition in GaN_yAs_{1-y}, $GaAs_{1-x}Bi_x$ and $GaN_yAs_{1-x-y}Bi_x$ (lattice-matched to GaAs). Closed red circles (green squares) show the values of E_{CB} and E_{VB} (E_g) averaged at each composition over those calculated for a series of freestanding disordered 4096-atom supercells using the sp^3s^* tight-binding model. Error bars denote the standard deviation about these average values, computed from the corresponding energies for the distinct supercells considered at each composition. Solid (dashed) black lines show E_{CB} and E_{VB} (E_g) calculated using the 14-band **k·p** Hamiltonian. (d) The variation of E_g and Δ_{SO} with N composition y in $GaN_yAs_{0.982-y}Bi_{0.018}$ ($x = 1.8\%$), calculated using the 14-band **k·p** Hamiltonian (dashed and solid black lines, respectively), compared to the results of room-temperature spectroscopic ellipsometry (SE; closed green squares and circles) and photomodulated-reflectance (PR; closed red squares) measurements. The experimental data are from Ref. [73].

this giant band-gap bowing can be achieved in alloys that are lattice-matched to GaAs suggests significant potential for applications at infrared wavelengths. We note that (i) the decrease in E_{CB} is comparable to, but slightly larger than, that in GaN_yAs_{1-y} and (ii) the increase in E_{VB} is approximately equal to that in $GaAs_{1-x}Bi_x$. Δ_{SO} is calculated to increase by approximately 70 meV per percent Bi in lattice-matched $GaN_yAs_{1-x-y}Bi_x$—i.e., by approximately the same amount as in $GaAs_{1-x}Bi_x$—reflecting the weak impact of N incorporation on the VB structure.

As in Figs. 1(a) and 1(b), the error bars in Fig. 1(c) denote the standard deviations computed for E_{CB}, E_{VB} and E_g using the corresponding calculated values for the distinct supercells considered at each fixed alloy composition. As expected on the basis of the trends discussed above for ternary GaN_yAs_{1-y} and $GaAs_{1-x}Bi_x$ alloys, (i) the impact of N and Bi incorporation leads to large respective computed standard deviations in E_{CB} and E_{VB} and (ii) the magnitude of the computed standard deviation for E_{CB} at fixed composition is larger than that associated with E_{VB}. We note, then, that the standard deviation associated with E_g, the maximum calculated value of which was 98 meV at $x = 3.9\%$, is typically larger in $GaN_yAs_{1-x-y}Bi_x$ than that in either GaN_yAs_{1-y} or $GaAs_{1-x}Bi_x$ having the same N or Bi composition, but is in general broadly comparable in magnitude to that associated with GaN_yAs_{1-y}. Overall, these results reaffirm that N- and Bi-related alloy disorder leads to significant inhomogeneous spectral broadening of the band-edge transitions in GaN_yAs_{1-y} and $GaAs_{1-x}Bi_x$ alloys and demonstrates that while alloy disorder effects can be expected to have an important impact on the $GaN_yAs_{1-x-y}Bi_x$ electronic structure, the magnitude of such effects should somewhat exceed but nonetheless be broadly comparable to those in GaN_yAs_{1-y}.

To confirm that these trends can be described as a direct combination of the separate impact of N (Bi) incorporation primarily on the CB (VB) structure, we have also used the 14-band **k·p** model to calculate the composition-dependent band-edge energies. The results of the **k·p** calculations of E_{CB} and E_{VB} (solid black lines) and E_g (dashed black lines) for GaN_yAs_{1-y}, $GaAs_{1-x}Bi_x$ and $GaN_yAs_{1-x-y}Bi_x$ are shown, respectively, in Figs. 1(a), 1(b), and 1(c). In GaN_yAs_{1-y} ($GaAs_{1-x}Bi_x$), this corresponds to a 10- (12-) band **k·p** model of the band structure. In all cases, we note that the variation of E_{CB} and E_{VB} with composition is in good overall agreement with the results of the disordered supercell calculations. We note some minor deviation between the calculated variation of E_g in GaN_yAs_{1-y} and $GaN_yAs_{1-x-y}Bi_x$ using the TB and **k·p** models, which we identify as being associated with the relatively stronger impact of N-related cluster states—neglected in the **k·p** model—on the CB edge [23,39,48]. These results suggest overall that the evolution of the main features of the $GaN_yAs_{1-x-y}Bi_x$ band structure (i) is primarily determined by the influence of localized states associated with independent N and Bi impurities and (ii) can be reliably described using an extended **k·p** Hamiltonian the basis of which explicitly includes these localized states and their coupling to the GaAs host-matrix band edge states.

Finally, Fig. 1(d) compares the variation of E_g (solid black lines) and Δ_{SO} (dashed black lines) with N composition y, calculated using the 14-band **k**·**p** model, to photomodulated-reflectance (PR) and spectroscopic-ellipsometry (SE) measurements undertaken on a series of pseudomorphically strained $GaN_yAs_{0.982-y}Bi_{0.018}$ ($x = 1.8\%$) samples grown on GaAs via metal-organic vapor-phase epitaxy [73]. The calculated variation of E_g and Δ_{SO} with y is in good overall agreement with experiment. First, the 14-band model accurately describes the measured large reduction in E_g compared to that in GaAs and captures the evolution of E_g with increasing N composition. Second, the 14-band model describes well the overall magnitude of Δ_{SO}—which is larger than that in GaAs due to the presence of Bi—and that the incorporation of N tends to have little impact on Δ_{SO}, with the measured and calculated values remaining approximately constant across the range of N compositions considered, confirming the predicted weak impact of N incorporation on the VB structure.

C. The electronic properties of $GaN_yAs_{1-x-y}Bi_x$/GaAs quantum wells

In order to realize photonic devices based on $GaN_yAs_{1-x-y}Bi_x$ alloys, in practice there will likely be a need to develop quantum-confined heterostructures. We therefore elucidate and analyze the general features of the electronic and optical properties of $GaN_yAs_{1-x-y}Bi_x$/GaAs QWs, focusing in particular on the bound lowest-energy electron and highest-energy hole states $e1$ and $h1$. In order to account for alloy disorder effects, for each QW structure having fixed N and Bi composition, we consider ten distinct supercells having statistically different spatial random distributions (RDs) of substitutional N and Bi atoms at anion lattice sites in the $GaN_yAs_{1-x-y}Bi_x$ QW layer. We compare the results of atomistic TB calculations to those obtained for the same structures using the continuum 14-band **k**·**p** model in the envelope function approximation (EFA), in which the QWs are treated as idealized one-dimensional structures. Since the 14-band model does not explicitly account for the presence of alloy disorder, the results of the **k**·**p** calculations provide a reference against which to highlight the role played by alloy disorder in the full atomistic calculations.

Four compressively strained QW structures are considered: structures 1 and 2 are N-free $GaAs_{1-x}Bi_x$/GaAs QWs having respective Bi compositions $x = 6.25$ and 9%, while structures 3 and 4 are $GaN_yAs_{1-x-y}Bi_x$/GaAs QWs having respective Bi and N compositions $x = 6.25\%$, $y = 2.5\%$, and $x = 9\%$, $y = 1\%$. These structures are described in Table II and the simulated geometries are as described in Sec. II A. The N and Bi compositions for structures 3 and 4 are chosen to produce ground-state $e1$-$h1$ transition energies close to 0.8 eV, so as to analyze the QW properties in the composition ranges of interest for applications in the technologically important 1.55 μm wavelength range. Table II also summarizes the results of the 14-band **k**·**p** calculations for each QW structure, including the in-plane compressive strain ϵ_{xx}, CB and VB offsets ΔE_{CB} and ΔE_{HH}, and QW band gaps ($e1$-$h1$ transition energies). Based on our analysis in Sec. III B, we conclude that $GaN_yAs_{1-x-y}Bi_x$/GaAs heterostructures have large type-I band offsets and can therefore be expected to possess intrinsically high electron-hole spatial overlap, suggesting the possibility of achieving good optical efficiency and indicating the potential for the development of light-emitting and/or -absorbing devices. We calculate the respective CB and VB offsets $\Delta E_{CB} = 106$ meV and $\Delta E_{HH} = 359$ meV in structure 1 ($x = 6.25\%$), compared with 153 and 456 meV in structure 2 ($x = 9\%$). In these N-free structures, Bi incorporation brings about compressive strain and large VB offsets ΔE_{HH} and while ΔE_{CB} is considerably smaller it is nonetheless sufficiently large to provide good confinement of electrons and holes to facilitate efficient photon emission and/or absorption [31].

Beginning with structure 1 and incorporating 2.5% N in the QW layer to obtain structure 3 increases the ground-state transition wavelength by approximately 450 nm to 1.55 μm, while simultaneously reducing the net compressive strain by a factor of approximately 3 to $\epsilon_{xx} = -0.23\%$. Comparing the calculated band offsets for structures 1 and 3, we observe that N incorporation significantly increases ΔE_{CB}, by a factor of approximately 4 to 419 meV, corresponding to the strong N-induced reduction of the QW CB-edge energy. The VB offset is effectively unchanged, again reflecting the fact that N incorporation has little effect on the VB. We observe a similar trend in incorporating 1% N to go from structure 2 to structure 4. In all cases, we find that the trends in the net macroscopic

TABLE II. Details of the $GaN_yAs_{1-x-y}Bi_x$/GaAs structures analyzed in Secs. III C and III D. Structures 1 and 2 contain ternary (N-free) $GaAs_{1-x}Bi_x$/GaAs QWs, while structures 3 and 4 contain quaternary $GaN_yAs_{1-x-y}Bi_x$ QWs. In addition to the Bi and N compositions x and y, we summarize the results of the 14-band **k**·**p** calculations, which are independent of alloy disorder at fixed composition. We provide the computed in-plane component ϵ_{xx} ($= \epsilon_{yy}$, compressive in all structures) of the macroscopic strain, as well as the CB- and VB-band offsets (ΔE_{CB} and ΔE_{HH}), the ground-state transition energy $e1$-$h1$ at $T = 300$ K, and the corresponding ground-state emission and/or absorption wavelength for the $e1$-$h1$ transition.

Structure	x (%)	y (%)	ϵ_{xx} (%)	ΔE_{CB} (meV)	ΔE_{HH} (meV)	$e1$-$h1$ (eV)	$e1$-$h1$ (nm)
1	6.25	—	−0.74	106	359	1.097	1130
2	9.00	—	−1.06	153	456	0.960	1292
3	6.25	2.50	−0.23	419	366	0.791	1568
4	9.00	1.00	−0.86	306	459	0.808	1535

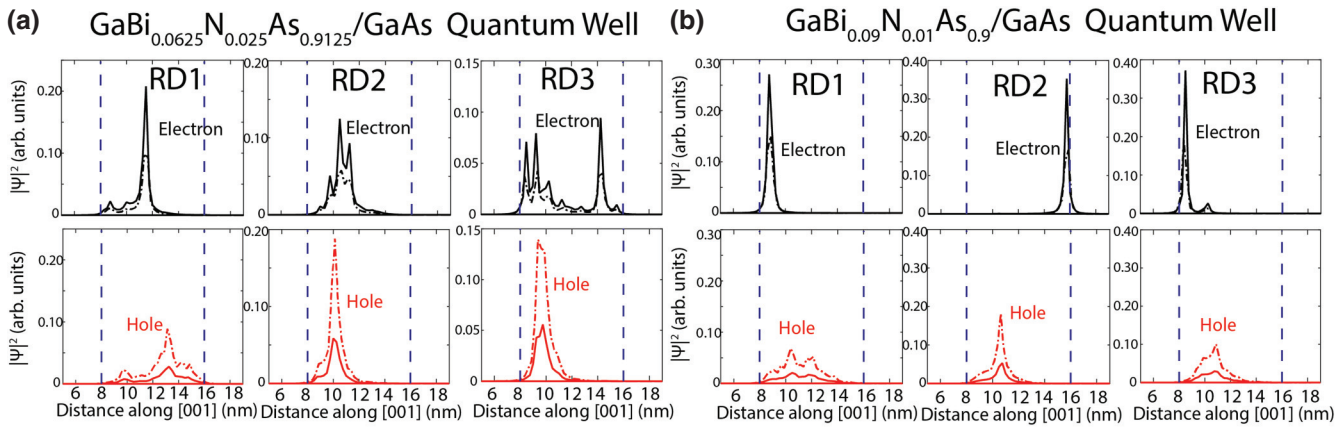


FIG. 2. The probability density associated with the lowest-energy CB electron state ($e1$; upper row) and the highest-energy VB hole state ($h1$; lower row) in 8-nm-thick (a) $GaN_{0.025}As_{0.9125}Bi_{0.0625}/GaAs$ ($x = 6.25\%$, $y = 2.5\%$) and (b) $GaN_{0.01}As_{0.90}Bi_{0.09}/GaAs$ ($x = 9\%$, $y = 1\%$) QWs. Solid (dash-dotted) black lines and solid (dash-dotted) red lines, respectively, denote the $e1$ and $h1$ probability densities at cation (anion) sites calculated using the TB model, obtained at each position z along the [001] growth direction by summing over the probability densities associated with each atom in the plane. Dashed blue lines denote the well-barrier interfaces. The TB calculations are performed for ten supercells containing different random spatial distributions (RDs) of substitutional N and Bi atoms on the anion sublattice: results are presented here for three representative structures in each case, with plots for additional $GaN_yAs_{1-x-y}Bi_x/GaAs$ structures, as well as for $GaAs_{1-x}Bi_x/GaAs$ structures, provided in Figs. 5 and 6 of the Supplemental Material [50].

strain, the QW band offsets, and the band gap calculated using the 14-band model are consistent with those obtained from the full atomistic calculations.

Figures 2(a) and 2(b) show the probability density for the $e1$ (upper panels; black lines) and $h1$ (lower panels; red lines) states in the $GaN_yAs_{1-x-y}Bi_x/GaAs$ QW structures (a) 3 and (b) 4, calculated using the TB method. For each structure, we have plotted probability densities for three of the ten different RDs of Bi and N atoms considered; plots for additional RDs can be found in Fig. 6 of the Supplemental Material [50]. The solid and dashed lines, respectively, denote the probability density projected to cations and anions, calculated using the TB method at each fixed position z along [001] by summing over the probability density associated with all atoms in the plane perpendicular to [001]. First, we note that the calculated probability densities in the N-free QWs, structures 1 and 2—which, for brevity, are provided in Sec. 3 of the Supplemental Material [50]—demonstrate that short-range alloy disorder strongly perturbs the hole states in $GaAs_{1-x}Bi_x/GaAs$ QWs, while the electron states in the relatively unperturbed CB can be well described using the conventional EFA. The $GaN_yAs_{1-x-y}Bi_x/GaAs$ $h1$ probability densities calculated using the TB method are qualitatively the same as those in the N-free structures—as expected, given the weak impact of N incorporation on the VB structure. The $h1$ eigenstates depart from a conventional envelope-function–like behavior: we calculate that, in a given structure, $h1$ tends to localize preferentially within the QW about regions of locally high Bi composition—i.e., about pairs and larger clusters of Bi atoms. In the CB, we note that introducing N brings about a marked qualitative change in the nature of the $e1$ eigenstates: the $e1$ probability density in the presence of N mirrors that of $h1$ in the presence of Bi, reflecting the fact that N localized states strongly perturb the CB structure. As we have identified in our previous analysis of the GaN_yAs_{1-y} ($GaAs_{1-x}Bi_x$) electronic structure, the observed strong localization of the CB- (VB-) edge eigenstates generally reflects strong hybridization of the extended GaAs band edge states with a multiplicity of N (Bi) localized states associated with pairs and larger clusters of substitutional N (Bi) impurities, resulting in significant degradation of the Bloch character of the corresponding alloy eigenstates [27,48,49]. In the $GaN_yAs_{1-x-y}Bi_x$ QW structures considered here, this behavior is reflected in the near-complete breakdown of the EFA description of the carrier probability densities due to strong electron and hole localization, with the details of the QW electronic properties being strongly dependent on the precise nature of the short-range alloy disorder present in the $GaN_yAs_{1-x-y}Bi_x$ layer of the structure.

Figures 3(a)–3(d) provide a summary of the calculated $e1$ and $h1$ probability densities for structures 1–4 respectively, using both the TB (solid and dashed black and red lines) and 14-band **k**·**p** (solid and dashed green lines) models. The probability densities shown for the TB calculations are averaged over those computed for the ten different supercells (RDs) used to represent each structure. As in our analysis of the bulk electronic structure (cf., Sec. III B), we find that the **k**·**p** method reliably captures the general trends observed in the full atomistic calculations. However, on average, alloy disorder effects cause a breakdown

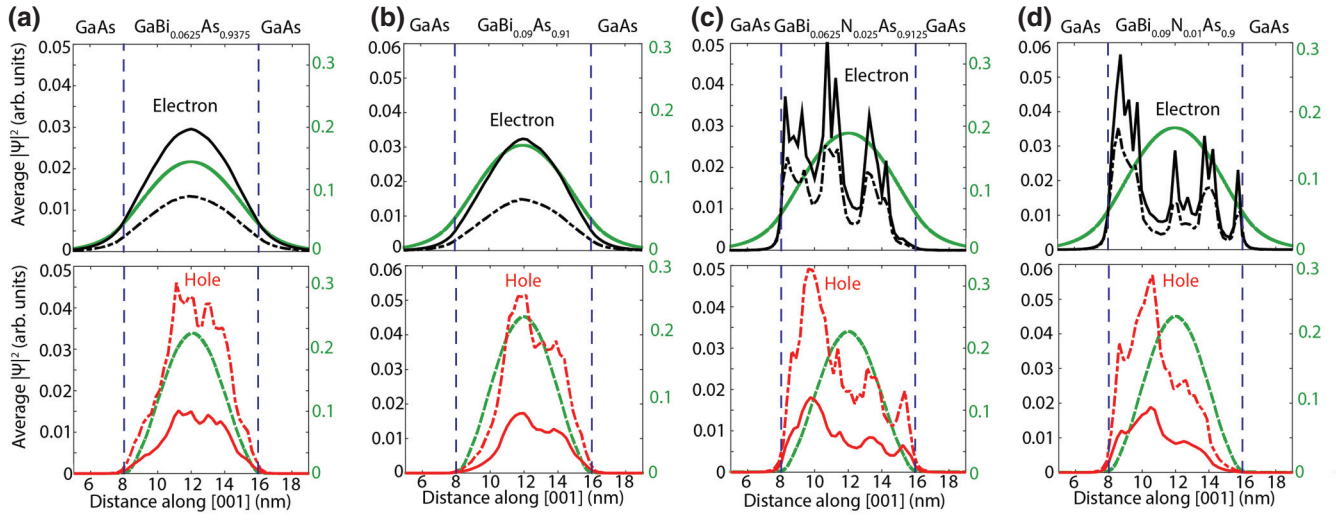


FIG. 3. The probability densities associated with the $e1$ (upper row) and $h1$ (lower row) states in structures (a) 1, (b) 2, (c) 3, and (d) 4 of Table II. Solid (dash-dotted) black and red lines denote the electron and hole probability densities at cation (anion) sites, calculated using the TB model and averaged over the ten different RDs considered for each structure. Solid (dashed) green lines denote the $e1$ ($hh1$) probability density calculated using the 14-band **k·p** Hamiltonian in the EFA. Dashed blue lines denote the well-barrier interfaces.

of the EFA for hole states in $GaAs_{1-x}Bi_x$ QWs, and for both electron and hole states in $GaN_yAs_{1-x-y}Bi_x$ QWs. On this basis, we conclude that the electronic properties of $GaN_yAs_{1-x-y}Bi_x$/GaAs QWs are strongly influenced by the alloy microstructure and hence that the bound states in $GaN_yAs_{1-x-y}Bi_x$ heterostructures are generally characterized by strong localization and a corresponding degradation in Bloch character, compared to those in equivalent structures based on conventional semiconductor alloys.

D. Optical transitions in $GaN_yAs_{1-x-y}Bi_x$/GaAs quantum wells

We now consider the optical properties of these QW structures and, again facilitated by comparison with the results of the atomistic TB and continuum **k·p** calculations, quantify the impact of alloy disorder on the QW band gap and ground-state optical transition strengths.

The results of our TB calculations of the optical properties for structures 1–4 are summarized in Figs. 4(a)–4(d), respectively, where, in each case, the results for all ten different RDs are shown. The solid black (red) lines show the computed TE- (TM-)polarized $e1$-$h1$ optical transition strengths, plotted in each case at the wavelength λ corresponding to the computed $e1$-$h1$ transition energy. We begin by noting that since all QWs considered are compressively strained, in the **k·p** calculations $h1$ is purely HH-like at the QW zone center ($\mathbf{k}_{\|} = 0$). As such, the $h1$ eigenstates computed using the 14-band model have no component along the [001] direction, so that the zone-center TM-polarized optical transition strength vanishes in accordance with the conventional selection rules for QWs. Examining the results of the atomistic calculations in Figs. 4(a) and 4(b), we note that this selection rule holds generally in the N-free $GaAs_{1-x}Bi_x$/GaAs structures 1 and 2: the calculated TM-polarized optical transition strengths are negligibly small, even in the presence of significant alloy disorder at $x = 9\%$ [60].

The calculated TE-polarized optical transition strengths for structures 1 and 2 describe that the band-edge optical transitions in $GaAs_{1-x}Bi_x$/GaAs QWs are characterized by inhomogeneous broadening associated with alloy-disorder-induced fluctuations in the QW band gap [49,60], producing a spectral width $\Delta\lambda$ of the $e1$-$h1$ transition wavelength—computed as the standard deviation of the $e1$-$h1$ wavelengths for the ten different RDs used to represent each QW—of 10 nm (17 nm) at $x = 6.25\%$ (9%) [49,60]. The TB calculations indicate little degradation in the optical transition strengths in going from structure 1 to 2, reflecting the fact that the slight reduction in the Bloch character of $h1$ associated with this approximately 3% increase in x is offset by the increase in electron-hole spatial overlap brought about by the accompanying increase in ΔE_{CB} [31,49,60]. Indeed, the **k·p** calculations for structures 1 and 2 indicate a modest increase $\lesssim 5\%$ in the TE-polarized optical transition strength in going from $x = 6.25$ to 9%: we attribute the deviation from this trend observed in the TB calculations to the impact of alloy disorder on the $h1$ eigenstates, with the formation of pairs and larger clusters of Bi atoms acting to decrease the Bloch character of the VB edge states. We note that these trends are consistent with the available experimental data, as highlighted in our previous analysis of bulk $GaAs_{1-x}Bi_x$ alloys and QWs.

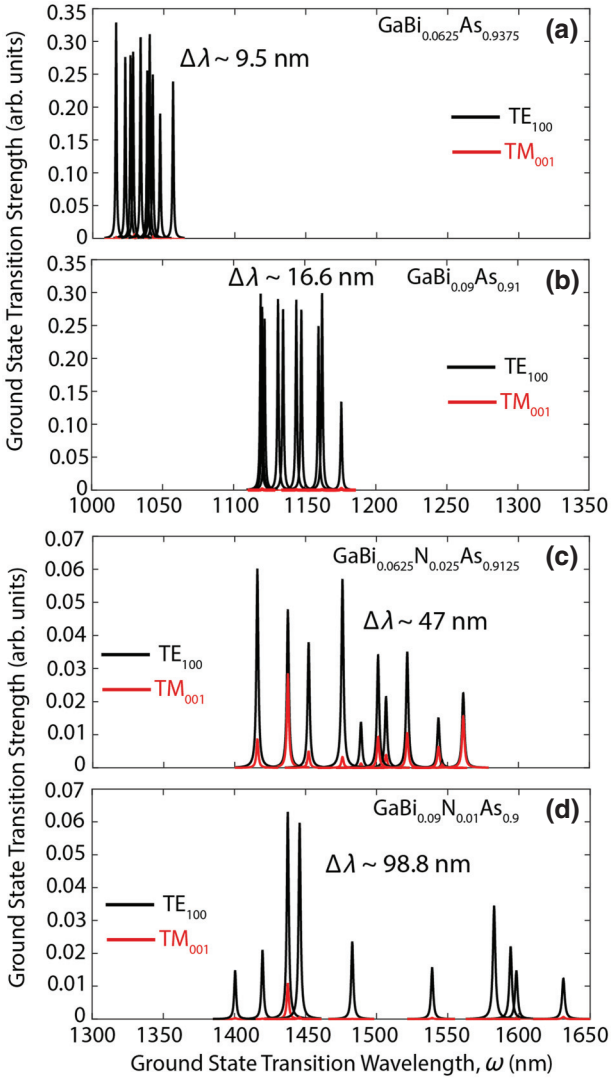


FIG. 4. The TE-polarized (solid black lines) and TM-polarized (solid red lines) optical transition strengths between the $e1$ and $h1$ states, calculated using the atomistic TB model, for the N-free $GaAs_{1-x}Bi_x$/GaAs QW structures (a) 1 and (b) 2 and for the $GaN_yAs_{1-x-y}Bi_x$/GaAs QW structures (c) 3 and (b) 4 (cf., Table II). For each structure, the computed transition strengths are shown for all ten distinct supercells considered. The spectral width of the ground-state transition wavelength ($\Delta\lambda$) is calculated as the standard deviation of the wavelengths computed for the ten distinct supercells (RDs) used to represent each structure.

Turning our attention to the quaternary QWs—structures 3 and 4—in Figs. 4(c) and 4(d), we note that coalloying N and Bi leads to significant modifications of the optical properties. First, we note a breakdown of the conventional QW selection rules: the $h1$ eigenstates in certain supercells acquire appreciable LH character in the presence of N, leading to nonzero zone-center TM-polarized $e1$-$h1$ optical transition strengths. Our calculations identify this as being primarily a result of the impact of local regions of tensile strain—due to lattice relaxation about N atomic sites—on the bound-hole states. These microscopic regions of tensile strain allow the predominantly HH-like $h1$ eigenstates to acquire an admixture of LH character—i.e., p-like orbital components polarized along the growth direction—and hence to have nonzero transition strengths at the zone center for TM-polarized transitions involving $e1$. While N incorporation leaves the overall character of the VB edge states largely unchanged, on average, this demonstrates that N clustering can nonetheless bring about nontrivial modification of the character of individual bound-hole states. This further confirms that calculated breakdown of the conventional optical selection rules is associated with the impact of N-related alloy disorder on the VB structure. This explicitly local effect is not accounted for in the 14-band **k**·**p** model considered here, nor in existing models of the $GaN_yAs_{1-x-y}Bi_x$ band structure. We note, however, that this calculated breakdown of the conventional QW optical selection rules does not necessarily imply that measured optical spectra for $GaN_yAs_{1-x-y}Bi_x$-based QWs will have large TM-polarized components. Our analysis here focuses on individual QW eigenstates: more detailed analysis shows that this behavior is associated with the formation of localized states about clusters of N atoms, which occur relatively rarely and are hence unlikely to contribute significantly to the net optical emission and/or absorption.

Second, we note that the combination of N- and Bi-related alloy disorder leads to large variations of the QW band gap between the distinct supercells considered for each structure, resulting in $\Delta\lambda = 47$ nm (99 nm) in structure 3 (4). For some RDs, we calculate anomalously low ground-state optical transition strengths, which our analysis associates with strong hybridization of the $e1$ ($h1$) eigenstates with N (Bi) cluster states that are typically strongly localized, spatially separated from one another, and lie close in energy to the bulk CB or VB edge. We note that the degradation in Bloch character that this represents is also manifest through the strong calculated decrease in optical transition strength due to the incorporation of N at fixed x (i.e., in going from structure 1 to 3 or structure 2 to 4). The **k**·**p** calculations indicate that the TE-polarized optical transition strength in structure 3 (structure 4) should be approximately 75% (approximately 80%) of that in structure 1 (structure 2), underestimating the approximately fivefold reduction observed in the full atomistic calculations: the extended nature of the QW eigenstates calculated in the EFA does not capture the impact of carrier localization about N and/or Bi clusters on the $e1$-$h1$ spatial overlap. This discrepancy highlights the role played by short-range alloy disorder in determining the optical properties of $GaN_yAs_{1-x-y}Bi_x$-based heterostructures and indicates that intrinsic alloy disorder may potentially limit the optical efficiency and performance of real $GaN_yAs_{1-x-y}Bi_x$ materials and devices.

The calculated strong variation of the TE-polarized optical transition strengths for the distinct RDs considered

reaffirms that the large number of mixed-anion local environments that occur in a randomly disordered $GaN_yAs_{1-x-y}Bi_x$ alloy has a significant impact on the band-edge eigenstates. In general, short-range alloy disorder generates a multiplicity of band edge states that are (i) spread over a relatively small range of energies and (ii) strongly localized, at different locations in the different QW structures investigated. In a real $GaN_yAs_{1-x-y}Bi_x$ heterostructure, the band-edge optical emission and/or absorption will then consist of contributions from a range of such states, having broadly similar character to the $e1$ and $h1$ states described above. Previous analysis has demonstrated that the net electronic and optical properties arising from such states can be accounted for using EFA-based models by including an appropriate description of the associated inhomogeneous spectral broadening, at least in type-I heterotructures [31,75]. This has allowed, e.g., quantitative prediction of the optical gain in $(In)GaN_yAs_{1-y}$ $GaAs_{1-x}Bi_x$ QW laser structures [67,68]. As such, while full atomistic calculations demonstrate a breakdown of the EFA for individual eigenstates in $GaN_yAs_{1-x-y}Bi_x$, and are required in general to understand the full details of the unusual material properties, it is possible that EFA-based models may provide an average description of the electronic and optical properties that accurately describes the measured trends in real heterostructures. However, the stronger localization of electrons in the N-containing QWs [cf., Figs. 3(c) and 3(d)] suggests that the EFA may overestimate the carrier spatial overlap in type-II $GaN_yAs_{1-y}/GaAs_{1-x}Bi_x$ QW structures.

Overall, our results indicate that short-range alloy disorder has a marked impact on the $GaN_yAs_{1-x-y}Bi_x$ alloy properties, similar in nature to equivalent effects in $Ga(In)N_yAs_{1-y}$ and $GaAs_{1-x}Bi_x$ alloys and heterostructures [31,75]. We expect that a similar **k·p**-based approach to that developed for $InGaN_yAs_{1-y}$ and $(In)GaAs_{1-x}Bi_x$ can be reliably applied to compute, analyze, and optimize the properties of devices based on type-I $GaN_yAs_{1-x-y}Bi_x$ heterostructures, but that detailed comparison to future experimental measurements will be required to ascertain the validity of such approaches when applied to type-II heterostructures based on N- and Bi-containing alloys [76].

IV. IMPLICATIONS FOR PRACTICAL APPLICATIONS

Having quantified key trends in the evolution of the $GaN_yAs_{1-x-y}Bi_x$ electronic and optical properties, we turn our attention to the consequences of the unusual material band structure for device applications. As we have demonstrated above that the 14-band **k·p** Hamiltonian describes the composition-dependent band-edge energies well, we employ this model to compute the dependence of the energy gaps on N and Bi composition and on epitaxial strain. These calculations are summarized in Fig. 5, where

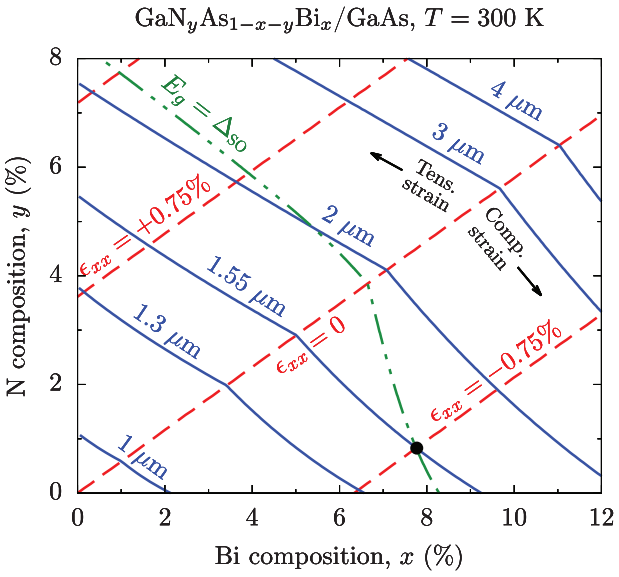


FIG. 5. A composition space map calculated using the 14-band **k·p** Hamiltonian, describing the variation of the in-plane strain ($\epsilon_{xx} = \epsilon_{yy}$) and room-temperature band gap (E_g) in pseudomorphically strained $GaN_yAs_{1-x-y}Bi_x$ alloys grown on [001]-oriented GaAs. The solid blue and dashed red lines, respectively, denote paths in the composition space along which E_g and ϵ_{xx} are constant. The dashed-dotted green line denotes alloy compositions for which $E_g = \Delta_{SO}$; alloys lying to the right of this contour have $\Delta_{SO} > E_g$ and are predicted to have suppressed CHSH Auger recombination and IVBA.

solid blue (dashed red) lines denote alloy compositions for which a fixed band gap E_g (strain ϵ_{xx}) can be achieved in pseudomorphically strained $GaN_yAs_{1-x-y}Bi_x/GaAs$. The $\epsilon_{xx} = 0$ line describes that lattice-matching to GaAs is achieved for $y = 0.58x$. The extremely strong reduction of E_g allows long emission and/or absorption wavelengths—ranging from approximately 1 μm through the near-infrared to midinfrared wavelengths in excess of 4 μm—to be achieved at N and Bi compositions compatible with established epitaxial growth [33,35,36,73,77,78].

The dash-dotted green line in Fig. 5 denotes alloy compositions for which $E_g = \Delta_{SO}$, so that alloys lying to the left (right) of this contour have $\Delta_{SO} < E_g$ ($\Delta_{SO} > E_g$). We recall that Auger recombination and IVBA processes involving the SO band play an important role in limiting the performance of near- and midinfrared light-emitting devices [19]. For processes involving the SO band, there are three distinct cases to consider: (i) $\Delta_{SO} < E_g$, (ii) $\Delta_{SO} = E_g$, and (iii) $\Delta_{SO} > E_g$. Case (i) is typical of near-infrared GaAs- and InP-based light-emitting devices operating at wavelengths between 0.9 and 1.7 μm. In this regime, CHSH Auger recombination and IVBA involving the SO band are present, with the magnitude of these effects increasing strongly as the difference $E_g - \Delta_{SO}$ decreases [79]. In GaAs-based devices operating close to 1

μm ($E_g = 1.24$ eV), one typically has $E_g - \Delta_{SO} \approx 0.90$ eV, with CHSH Auger recombination and IVBA each playing a minimal role. However, in InP-based devices operating at 1.55 μm ($E_g = 0.8$ eV), it is typical to have $E_g - \Delta_{SO} \approx 0.45$ eV, with CHSH Auger recombination and IVBA each assuming a dominant role in limiting device performance [15,80]. This trend has been clearly observed in temperature- and pressure-dependent experimental measurements performed on a range of InP-based devices, highlighting the fact that the threshold current density increases superlinearly with emission wavelength as one approaches case (ii) [81,82].

In case (ii), which is denoted by the closed black circle in Fig. 5, the CHSH Auger recombination and IVBA processes are resonant and can be expected to place severe limitations on efficiency, thereby all but eliminating the potential for sustainable device operation. For case (iii), an electron-hole pair recombining across the band gap provides insufficient energy to promote an electron from the SO band to a VB-edge hole state, thereby suppressing CHSH Auger recombination and IVBA by conservation of energy [18,82]. This is the case in GaSb-based midinfrared devices operating at wavelengths between 2 and 3 μm where, in line with the expected suppression of CHSH Auger recombination and IVBA, reduced threshold current densities compared to those in equivalent InP-based near-infrared devices are observed in experiment [82].

As such, there are two desirable scenarios from the perspective of the relationship between E_g and Δ_{SO}: first, when $\Delta_{SO} < E_g$ with the ratio $\frac{\Delta_{SO}}{E_g}$ significantly less than one, in which case CHSH Auger recombination and IVBA occur but at sufficiently low rates so as not to impede device performance; and second, the ideal scenario in which $\Delta_{SO} > E_g$ and CHSH Auger recombination and IVBA can be expected to be suppressed. While the ideal $\Delta_{SO} > E_g$ scenario can in principle be achieved in $GaAs_{1-x}Bi_x$ ($y = 0$) with $E_g = 1.55$ μm, our calculations show that incorporating N requires a reduction in x to maintain a fixed emission wavelength and therefore reduces Δ_{SO} relative to E_g—an undesirable change that pushes the band structure from case (iii) toward case (ii). N incorporation then quickly brings E_g and Δ_{SO} into resonance—i.e., case (ii), $E_g = \Delta_{SO}$—the worst possible scenario in terms of the suitability of the band structure for the development of a light-emitting device.

The results in Fig. 5 then indicate that N-free $GaAs_{1-x}Bi_x$ alloys provide the ideal scenario for the realization of efficient light emission at 1.55 μm and that coalloying N with Bi to achieve 1.55 μm emission presents a band structure that is not compatible with the design of light-emitting devices. As a result of the strong increase in Δ_{SO} brought about by Bi incorporation, at 1.3 μm alloys containing Bi will have $\Delta_{SO} < E_g$ but with the difference $E_g - \Delta_{SO}$ being smaller than in a conventional InP-based material. This suggests that increased losses due to CHSH Auger recombination and IVBA can be expected in a 1.3 μm GaAs-based $GaN_yAs_{1-x-y}Bi_x$ device compared to a conventional InP-based device operating at the same wavelength.

Additionally, we note that it is generally desirable to exploit strain in QW lasers to enhance performance via reduction of the density of states close in energy to the VB edge (in compressively strained structures) or via polarization selectivity (in tensile strained structures) [17,83]. At a fixed emission wavelength, one usually seeks to utilize an alloy that has as large a strain $|\epsilon_{xx}|$—compressive or tensile—as is compatible with epitaxial growth. The decrease in compressive strain compared to that in $GaAs_{1-x}Bi_x$ associated with incorporating N while maintaining a fixed emission wavelength can be expected to reduce the performance of a QW laser structure compared to that expected for an equivalent $GaAs_{1-x}Bi_x$/GaAs laser structure [31]. Therefore, the expected degradation in the suitability of the band structure in utilizing quaternary $GaN_yAs_{1-x-y}Bi_x$ in favor of (i) a conventional InP-based $(Al)In_{1-x}Ga_xAs$ heterostructure to achieve 1.3 μm emission or (ii) a ternary $GaAs_{1-x}Bi_x$ heterostructure to achieve 1.55 μm emission suggests, contrary to recent analysis [43,45], that $GaN_yAs_{1-x-y}Bi_x$ alloys and heterostructures containing N are *not* suitable for applications at 1.3 or 1.55 μm.

Our analysis does, however, confirm the potential of $GaN_yAs_{1-x-y}Bi_x$ alloys for applications in multijunction solar cells [46], since $E_g \approx 1$ eV can be achieved in alloys that can be grown lattice-matched to either GaAs or Ge ($y = 0.58x$, $x \approx 2.9\%$). While the difference $E_g - \Delta_{SO}$ for such alloys would not be as favorable as in an InP-based material designed to have a similar absorption wavelength, it is expected to be sufficiently large so as not to impede performance. Furthermore, the carrier densities present in an illuminated solar cell are significantly lower than those in an electrically pumped semiconductor laser, making Auger recombination—which scales roughly as the cube of the injected carrier density—less of an impediment to device operation. The modest N and Bi compositions required to reach a band gap of approximately 1 eV have been achieved in initial growth studies of $GaN_yAs_{1-x-y}Bi_x$/GaAs epitaxial layers [33,35,36,73,77,78]. Analysis of prototypical $GaAs_{1-x}Bi_x$/GaAs QW solar cells indicates that one potential factor limiting the photovoltaic performance of lattice-matched $GaN_yAs_{1-x-y}Bi_x$ junctions may be the large inhomogeneous spectral broadening of the band-edge optical absorption, associated with the presence of short-range alloy disorder and crystalline defects [84]. However, we expect that these issues could be mitigated to some degree via a combination of refinement of the epitaxial growth [85,86], sample preparation [87,88] and device design. This approach has been successfully employed to develop multijunction solar cells incorporating the dilute nitride

alloy (In)GaN_yAs_{1-y}, which have demonstrated record-breaking efficiency [89].

Finally, since our calculations indicate that $GaN_yAs_{1-x-y}Bi_x$ alloys display effectively identical enhancement of the spin-orbit coupling to that in $GaAs_{1-x}Bi_x$, similarly large enhancement of the Rashba spin-orbit interaction [90] to that in $GaAs_{1-x}Bi_x$ can be expected in $GaN_yAs_{1-x-y}Bi_x$, potentially opening up applications in spintronic devices [91].

V. CONCLUSIONS

We develop a multiscale theoretical framework to calculate the properties of $GaN_yAs_{1-x-y}Bi_x$ highly mismatched alloys and heterostructures, based on carefully derived atomistic TB and continuum **k·p** Hamiltonians. We perform a systematic investigation revealing key trends in the electronic and optical properties of bulk $GaN_yAs_{1-x-y}Bi_x$ alloys and $GaN_yAs_{1-x-y}Bi_x$/GaAs QWs. Our analysis indicates that $GaN_yAs_{1-x-y}Bi_x$ alloys provide broad scope for band-structure engineering: the incorporation of N (Bi) allows us to manipulate the CB (VB) structure close in energy to band edges, offering significant control over the band gap, the VB spin-orbit splitting energy, and the band offsets. Since the incorporation of N (Bi) brings about tensile (compressive) strain with respect to a GaAs substrate, coalloying N and Bi then further delivers significant control over the strain in epitaxial layers and heterostructures, providing further opportunities to tailor the electronic and optical properties. The intrinsic flexibility of the $GaN_yAs_{1-x-y}Bi_x$ alloy band structure is therefore particularly appealing for practical applications.

Through systematic analysis of large-scale atomistic electronic structure calculations, we demonstrate that the respective impacts of N and Bi incorporation on the CB and VB structure remain effectively independent, even in the presence of significant short-range alloy disorder. Comparison of atomistic and continuum calculations highlights the fact that a 14-band **k·p** Hamiltonian is sufficient to describe the evolution of the main features of the $GaN_yAs_{1-x-y}Bi_x$ band structure, with the predicted evolution of the band gap and VB spin-orbit splitting energy being in good agreement with experimental measurements. Application of the TB model to compute the electronic and optical properties of realistically sized $GaN_yAs_{1-x-y}Bi_x$/GaAs QWs demonstrates that short-range alloy disorder produces strong carrier localization, ultimately leading to significant inhomogeneous spectral broadening as well as a breakdown of the conventional selection rules governing QW optical transitions. On this basis, we conclude that alloy disorder effects are likely to play an important role in determining the properties of real $GaN_yAs_{1-x-y}Bi_x$ alloys and heterostructures. While our analysis suggests that **k·p**-based models incorporating appropriately parametrized inhomogeneous spectral broadening are likely to be suitable when applied to type-I heterostructures, further detailed analysis of N- and Bi-containing type-II heterostructures—e.g., GaN_yAs_{1-y}/$GaAs_{1-x}Bi_x$ QWs—may require a theoretical description based upon direct atomistic calculations.

Based on our analysis of the electronic structure, we discuss the implications of the unusual properties of $GaN_yAs_{1-x-y}Bi_x$ alloys for practical applications. Contrary to the existing literature, our analysis suggests that $GaN_yAs_{1-x-y}Bi_x$ heterostructures are not suitable for the development of GaAs-based semiconductor lasers operating at 1.3 or 1.55 μm: the reduction in compressive strain and spin-orbit splitting energy compared to equivalent N-free $GaAs_{1-x}Bi_x$ structures is expected to compromise the proposed benefits of Bi incorporation and hence place significant limitations on performance. Overall, we conclude that the features of the electronic structure revealed through our analysis indicate that $GaN_yAs_{1-x-y}Bi_x$ alloys are most promising as a suitable approximately 1 eV band-gap material for applications in multijunction solar cells, where they can provide GaAs- and Ge-compatible lattice- and current-matched junctions.

ACKNOWLEDGMENTS

M.U. and C.A.B. contributed equally to this work. This work was supported by the European Commission (Project No. FP7-257974), by Science Foundation Ireland (SFI; Project No. 15/IA/3082), and by the Engineering and Physical Sciences Research Council, U.K. (EPSRC; Project No. EP/K029665/1). M.U. acknowledges the use of computational resources from the National Science Foundation (NSF, USA) funded Network for Computational Nanotechnology (NCN) through http://nanohub.org. This work was supported by the computational resources provided by the Pawsey Supercomputing Center (Magnus cluster) through the National Computational Merit Allocation Scheme (NCMAS). We thank Dr. Zoe L. Bushell and Professor Stephen J. Sweeney of the University of Surrey, United Kingdom, for useful discussions and for providing access to the results of their experimental measurements prior to publication.

[1] M. Arai, W. Kobayashi, and M. Kohtoku, 1.3-μm-range metamorphic InGaAs laser with high characteristic temperature for low power consumption operation, IEEE J. Sel. Top. Quantum Electron. **19**, 1502207 (2013).

[2] R. Nakao, M. Arai, W. Kobayashi, T. Yamamoto, and S. Matsuo, 1.3-μm InGaAs MQW metamorphic laser diode fabricated with lattice relaxation control based on *in situ* curvature measurement, IEEE J. Sel. Top. Quantum Electron. **21**, 1501407 (2015).

[3] S. Bogusevschi, C. A. Broderick, and E. P. O'Reilly, Theory and optimization of 1.3 μm metamorphic quantum well lasers, IEEE J. Quantum Electron. **52**, 2500111 (2016).

[4] C. Berger, C. Möller, P. Hens, C. Fuchs, W. Stolz, S. W. Koch, A. Ruiz Perez, J. Hader, and J. V. Moloney, Novel type-II material system for laser applications in the near-infrared regime, AIP Adv. **5**, 047105 (2015).

[5] C. Lammers, M. Stein, C. Berger, C. Möller, C. Fuchs, A. Rahimi-Iman, W. Stolz, S. W. Koch, M. Koch, A. RuizPerez, J. Hader, and J. V. Moloney, Gain spectroscopy of a type-II VECSEL chip, Appl. Phys. Lett. **109**, 232107 (2016).

[6] C. Fuchs, C. Berger, C. Möller, M. Weseloh, S. Reinhard, J. Hader, J. V. Moloney, S. W. Koch, and W. Stolz, Electrical injection type-II (GaIn)As/Ga(AsSb)/(GaIn)As single "W"-quantum well laser at 1.2 μm, Electron. Lett. **52**, 1875 (2016).

[7] P. Michler, *Quantum Dots for Quantum Information Technologies* (Springer, New York, 2017).

[8] J. Wu and Z. M. Wang, *Quantum Dot Molecules: Lecture Notes in Nanoscale Science and Technology* (Springer, New York, 2013).

[9] D. Bimberg, N. Kirstaedter, N. N. Ledentsov, Zh. I. Alferov, P. S. Kop'ev, and V. M. Ustinov, InGaAs-GaAs quantum-dot lasers, IEEE J. Sel. Top. Quantum Electron. **3**, 196 (1997).

[10] D. L. Huffaker, G. Park, Z. Zou, O. B. Shchekin, and D. G. Deppe, 1.3 μm room-temperature GaAs-based quantum-dot laser, Appl. Phys. Lett. **73**, 2564 (1998).

[11] M. Usman, Atomistic theoretical study of electronic and polarization properties of single and vertically stacked elliptical InAs quantum dots, Phys. Rev. B **86**, 155444 (2012).

[12] M. Usman, V. Tasco, M. T. Todaro, M. De Giorgi, E. P. O'Reilly, and G. Klimeck, The polarization response in InAs quantum dots: theoretical correlation between composition and electronic properties, Nanotechnology **23**, 165202 (2012).

[13] M. Usman, H. Ryu, I. Woo, D. S. Ebert, and G. Klimeck, Moving toward nano-TCAD through multimillion-atom quantum-dot simulations matching experimental data, IEEE Trans. Nanotechnol. **8**, 330 (2009).

[14] A. F. Phillips, S. J. Sweeney, A. R. Adams, and P. J. A. Thijs, The temperature dependence of 1.3- and 1.5-μm compressively strained InGaAs(P) MQW semiconductor lasers, IEEE J. Sel. Top. Quantum Electron. **5**, 401 (1999).

[15] S. J. Sweeney, A. R. Adams, M. Silver, E. P. O'Reilly, J. R. Watling, A. B. Walker, and P. J. A. Thijs, Dependence of threshold current on QW position and on pressure in 1.5 μm InGaAs(P) lasers, Phys. Status Solidi B **211**, 525 (1999).

[16] T. J. Houle, J. C. L. Yong, C. M. Marinelli, S. Yu, J. M. Rorison, I. H. White, J. K. White, A. J. Springthorpe, and B. Garrett, Characterization of the temperature sensitivity of gain and recombination mechanisms in 1.3-μm AlGaInAs MQW lasers, IEEE J. Quantum Electron. **41**, 132 (2005).

[17] A. R. Adams, Strained-layer quantum well lasers, IEEE J. Sel. Top. Quantum Electron. **17**, 1364 (2011).

[18] C. A. Broderick, M. Usman, S. J. Sweeney, and E. P. O'Reilly, Band engineering in dilute nitride and bismide semiconductor lasers, Semicond. Sci. Technol. **27**, 094011 (2012).

[19] I. P. Marko and S. J. Sweeney, Optical and electronic processes in semiconductor materials for device applications, Springer Ser. Mater. Sci. **203**, 253 (2014).

[20] J. Li and Z. Wang editors,*Bismuth-Containing Compounds* (Springer, xxx, 2013).

[21] W. Shan, W. Walukiewicz, J. W. Ager III, E. E. Haller, J. F. Geisz, D. H. Friedman, J. M. Olson, and S. R. Kurtz, Band Anticrossing in GaInNAs Alloys, Phys. Rev. Lett. **82**, 1221 (1999).

[22] P. R. C. Kent and A. Zunger, Theory of electronic structure evolution in GaAsN and GaPN alloys, Phys. Rev. B **64**, 115208 (2001).

[23] E. P. O'Reilly, A. Lindsay, P. J. Klar, A. Polimeni, and M. Capizzi, Trends in the electronic structure of dilute nitride alloys, Semicond. Sci. Technol. **24**, 033001 (2009).

[24] A. Janotti, S.-H. Wei, and S. B. Zhang, Theoretical study of the effects of isovalent coalloying of Bi and N in GaAs, Phys. Rev. B **65**, 115203 (2002).

[25] Y. Zhang, A. Mascarenhas, and L.-W. Wang, Similar and dissimilar aspects of III–V semiconductors containing Bi versus N, Phys. Rev. B **71**, 155201 (2005).

[26] W.-X. Deng, J. Li, S.-S. Li, H. Peng, J.-B. Xia, L.-W. Wang, and S.-H. Wei, Band crossing in isovalent semiconductor alloys with large size mismatch: First-principles calculations of the electronic structure of Bi and N incorporated GaAs, Phys. Rev. B **82**, 193204 (2010).

[27] M. Usman, C. A. Broderick, A. Lindsay, and E. P. O'Reilly, Tight-binding analysis of the electronic structure of dilute bismide alloys of GaP and GaAs, Phys. Rev. B **84**, 245202 (2011).

[28] B. Fluegel, S. Francoeur, A. Mascarenhas, S. Tixier, E. C. Young, and T. Tiedje, Giant Spin-Orbit Bowing in $GaAs_{1-x}Bi_x$, Phys. Rev. Lett. **97**, 067205 (2006).

[29] Z. Batool, K. Hild, T. J. C. Hosea, X. Lu, T. Tiedje, and S. J. Sweeney, The electronic band structure of GaBiAs/GaAs layers: Influence of strain and band anti-crossing, J. Appl. Phys. **111**, 113108 (2012).

[30] S. J. Sweeney and S. R. Jin, Bismide-nitride alloys: Promising for efficient light emitting devices in the near- and mid-infrared, J. Appl. Phys. **113**, 043110 (2013).

[31] C. A. Broderick, P. E. Harnedy, and E. P. O'Reilly, Theory of the electronic and optical properties of dilute bismide quantum well lasers, IEEE J. Sel. Top. Quant. Electron. **21**, 1503313 (2015).

[32] A. Mascarenhas, Y. Zhang, J. Verley, and M. J. Seong, Overcoming limitations in semiconductor alloy design, Superlattices Microstruct. **29**, 395 (2001).

[33] M. Yoshimoto, W. Huang, Y. Takehara, J. Saraie, A. Chayahara, Y. Horino, and K. Oe, New semiconductor GaNAsBi alloy grown by molecular beam epitaxy, Jpn. J. Appl. Phys. **43**, L845 (2004).

[34] W. Huang, M. Yoshimoto, Y. Takehara, J. Saraie, and K. Oe, $GaNGaN_yAs_{1-x-y}Bi_x$ alloy lattice matched to GaAs with 1.3 μm photoluminescence emission, Jpn. J. Appl. Phys. **43**, L1350 (2004).

[35] S. Tixier, S. E. Webster, E. C. Young, T. Tiedje, S. Francoeur, A. Mascarenhas, P. Wei, and F. Schiettekatte, Band gaps of the dilute quaternary alloys $GaN_yAs_{1-x-y}Bi_y$ and $Ga_{1-y}In_yN_xAs_{1-x}$, Appl. Phys. Lett. **86**, 112113 (2005).

[36] Z. L. Bushell, P. Ludewig, N. Knaub, Z. Batool, K. Hild, W. Stolz, S. J. Sweeney, and K. Volz, Growth and characterisation of Ga(NAsBi) alloy by metal-organic vapour phase epitaxy, J. Cryst. Growth **396**, 79 (2014).

[37] Y. Zhang, A. Mascarenhas, and L.-W. Wang, Non-Bloch Nature of Alloy States in a Conventional Semiconductor Alloy: $Ga_xIn_{1-x}P$ as an Example, Phys. Rev. Lett. **101**, 036403 (2008).

[38] S.-H. Wei and A. Zunger, Giant and Composition-Dependent Optical Bowing Coefficient in GaAsN Alloys, Phys. Rev. Lett. **76**, 664 (1996).

[39] C. A. Broderick, M. Seifikar, E. P. O'Reilly, and J. M. Rorison, in *Handbook of Optoelectronic Device Modeling and Simulation* (CRC Press, Boca Raton, FL, 2017), Vol. 1.

[40] C. A. Broderick, I. P. Marko, E. P. O'Reilly, and S. J. Sweeney, in *Handbook of Optoelectronic Device Modeling and Simulation* (CRC Press, Boca Raton, FL, 2017), Vol. 1.

[41] S. Nacer, A. Aissat, and K. Ferdjani, Band gap and band offsets of GaNAsBi lattice matched to GaAs substrate, Opt. Quant. Electron. **40**, 677 (2008).

[42] C. A. Broderick, M. Usman, and E. P. O'Reilly, Derivation of 12- and 14-band **k**·**p** Hamiltonians for dilute bismide and bismide-nitride alloys, Semicond. Sci. Technol. **28**, 125025 (2013).

[43] M. M. Habchi, C. Bilel, A. Ben Nasr, and B. El Jani, Self-consistent analysis of the band structure of doped lattice-matched GaNAsBi-based QWs operating at 1.55 μm, Mater. Sci. Semicond. Process. **28**, 108 (2014).

[44] Z.-G. Song, S. Bose, W.-J. Fan, and S.-S. Li, Electronic band structure and optical gain of $GaN_xBi_yAs_{1-x-y}$/GaAs pyramidal quantum dots, J. Appl. Phys. **119**, 143043 (2016).

[45] W. J. Fan, S. Bose, and D. H. Zhang, Electronic bandstructure and optical gain of lattice matched III-V dilute nitride bismide quantum wells for 1.55 μm optical communication systems, J. Appl. Phys. **120**, 093111 (2016).

[46] S. J. Sweeney, K. Hild, and S. R. Jin, in *Proceedings of the 39th IEEE Photovoltaics Specialists Conference* (2013).

[47] P. R. C. Kent, L. Bellaiche, and A. Zunger, Pseudopotential theory of dilute III-V nitrides, Semicond. Sci. Technol. **17**, 851 (2002).

[48] E. P. O'Reilly, A. Lindsay, and S. Fahy, Theory of the electronic structure of dilute nitride alloys: Beyond the band-anti-crossing model, J. Phys. Condens. Matter **16**, S3257 (2004).

[49] M. Usman, C. A. Broderick, Z. Batool, K. Hild, T. J. C. Hosea, S. J. Sweeney, and E. P. O'Reilly, Impact of alloy disorder on the band structure of compressively strained $GaBi_xAs_{1-x}$, Phys. Rev. B **87**, 115104 (2013).

[50] See the Supplemental Material at http://link.aps.org/supplemental/10.1103/PhysRevApplied.10.044024.

[51] E. P. O'Reilly and A. Lindsay, Tight-binding approach to calculation of localised perturbations in semiconductors, J. Phys.: Conf. Ser. **242**, 012002 (2010).

[52] A. Lindsay and E. P. O'Reilly, Unification of the Band Anticrossing and Cluster-State Models of Dilute Nitride Semiconductor Alloys, Phys. Rev. Lett. **93**, 196402 (2004).

[53] C. A. Broderick, S. Mazzucato, H. Carrère, T. Amand, H. Makhloufi, A. Arnoult, C. Fontaine, O. Donmez, A. Erol, M. Usman, E. P. O'Reilly, and X. Marie, Anisotropic electron $\boldsymbol{g}$ factor as a probe of the electronic structure of $GaBi_xAs_{1-x}$/GaAs epilayers, Phys. Rev. B **90**, 195301 (2014).

[54] S.-Y. Ren and W. A. Harrison, Semiconductor properties based upon universal tight-binding parameters, Phys. Rev. B **23**, 762 (1981).

[55] W. A. Harrison, New tight-binding parameters for covalent solids obtained using Louie peripheral states, Phys. Rev. B **24**, 5835 (1982).

[56] J. C. Slater and G. F. Koster, Simplified LCAO method for the periodic potential problem, Phys. Rev. **94**, 1498 (1954).

[57] A. Lindsay, Ph.D. thesis, University of Surrey2002.

[58] P. N. Keating, Effect of invariance requirements on the elastic strain energy of crystals with application to the diamond structure, Phys. Rev. **145**, 637 (1966).

[59] O. L. Lazarenkova, P. von Allmen, F. Oyafuso, S. Lee, and G. Klimeck, Effect of anharmonicity of the strain energy on band offsets in semiconductor nanostructures, Appl. Phys. Lett. **85**, 4193 (2004).

[60] M. Usman and E. P. O'Reilly, Atomistic tight-binding study of the electronic structure and interband optical transitions in $GaBi_xAs_{1-x}$/GaAs quantum wells, Appl. Phys. Lett. **104**, 071103 (2014).

[61] M. Usman, Large-scale atomistic simulations demonstrate dominant alloy disorder effects in GaBiAs/GaAs multiple quantum wells, Phys. Rev. Mater. **2**, 044602 (2018).

[62] K. Alberi, J. Wu, W. Walukiewicz, K. M. Yu, O. D. Dubon, S. P. Watkinsa, C. X. Wang, X. Liu, Y.-J. Cho, and J. Furdyna, Valence-band anticrossing in mismatched III–V semiconductor alloys, Phys. Rev. B **75**, 045203 (2007).

[63] A. Lindsay and E. P. O'Reilly, A tight-binding-based analysis of the band anti-crossing model in GaN_xAs_{1-x}, Physica E **21**, 901 (2004).

[64] Z. L. Bushell, C. A. Broderick, L. Nattermann, R. M. Joseph, J. M. Rorison, K. Volz, and S. J. Sweeney, Valence band-anticrossing in $GaP_{1-x}Bi_x$: Giant bowing of the band gap and spin-orbit splitting energy, arXiv:1710.08995v1 (2017).

[65] E. P. O'Reilly, A. Lindsay, S. Tomić, and M. Kamal-Saadi, Tight-binding and **k**·**p** models for the electronic structure of Ga(In)NAs and related alloys, Semicond. Sci. Technol. **17**, 870 (2002).

[66] A. Lindsay, S. Tomić, and E. P. O'Reilly, Derivation of a 10-band **k**·**p** model for dilute nitride semiconductors, Solid State Electron. **47**, 443 (2003).

[67] J. Hader, S. W. Koch, J. V. Moloney, and E. P. O'Reilly, Gain in 1.3 μm materials: InGaNAs and InGaPAs semiconductor quantum-well lasers, Appl. Phys. Lett. **77**, 630 (2000).

[68] I. P. Marko, C. A. Broderick, S. R. Jin, P. Ludewig, W. Stolz, K. Volz, J. M. Rorison, E. P. O'Reilly, and S. J. Sweeney, Optical gain in GaAsBi/GaAs quantum well diode lasers, Sci. Rep. **6**, 28863 (2016).

[69] P. R. C. Kent and A. Zunger, Evolution of III–V Nitride Alloy Electronic Structure: The Localized to Delocalized Transition, Phys. Rev. Lett. **86**, 2613 (2001).

[70] A. Lindsay and E. P. O'Reilly, A universal model for trends in A1-type defect states in zincblende and diamond semiconductor structures, Physica B **434**, 340 (2003).

[71] C. A. Broderick, M. Usman, and E. P. O'Reilly, 12-band k · p model for dilute bismide alloys of (In)GaAs derived

from supercell calculations, Phys. Status Solidi (b) **250**, 773 (2013).

[72] Lars C. Bannow, Stefan C. Badescu, Jörg Hader, Jerome V. Moloney, and Stephan W. Koch, Valence band splitting in bulk dilute bismides, arXiv:1709.09983 (2017).

[73] Z. L. Bushell, R. M. Joseph, L. Nattermann, P. Ludewig, K. Volz, J. L. Keddie, and S. J. Sweeney, Optical functions and critical points of dilute bismide alloys studied by spectroscopic ellipsometry, J. Appl. Phys. **123**, 045701 (2018).

[74] A. Lindsay and E. P. O'Reilly, Influence of nitrogen resonant states on the electronic structure of GaN_xAs_{1-x}, Solid State Commun. **118**, 313 (2001).

[75] S. Tomić, E. P. O'Reilly, R. Fehse, S. J. Sweeney, A. R. Adams, A. D. Andreev, S. A. Choulis, T. J. C. Hosea, and H. Riechert, Theoretical and experimental analysis of 1.3-μm InGaNAs/GaAs lasers, IEEE. J. Sel. Top. Quantum Electron. **9**, 1228 (2003).

[76] C. A. Broderick, S. R. Jin, I. P. Marko, K. Hild, P. Ludewig, Z. L. Bushell, W. Stolz, J. M. Rorison, E. P. O'Reilly, K. Volz, and S. J. Sweeney, $GaAs_{1-x}Bi_x/GaN_yAs_{1-y}$ type-II quantum wells: Novel strain-balanced heterostructures for GaAs-based near- and mid-infrared photonics, Sci. Rep. **7**, 46371 (2017).

[77] W. Huang, K. Oe, G. Feng, and M. Yoshimoto, Molecular-beam epitaxy and characteristics of $GaN_yAs_{1-x-y}Bi_x$, J. Appl. Phys. **98**, 053505 (2005).

[78] M. Yoshimoto, W. Huang, G. Feng, Y. Tanaka, and K. Oe, Molecular-beam epitaxy of GaNAsBi layer for temperature-insensitive wavelength emission, J. Cryst. Growth **301**, 975 (2007).

[79] M. Silver, E. P. O'Reilly, and A. R. Adams, Determination of the wavelength dependence of Auger recombination in long-wavelength quantum-well semiconductor lasers using hydrostatic pressure, IEEE J. Quantum Electron. **33**, 1557 (1997).

[80] S. J. Sweeney, A. F. Phillips, A. R. Adams, E. P. O'Reilly, and P. J. A. Thijs, The effect of temperature dependent processes on the performance of 1.5-μm compressively strained InGaAs(P) MQW semiconductor diode lasers, IEEE Photon. Tech. Lett. **10**, 1076 (1998).

[81] S. J. Sweeney, in *22nd IEEE International Semiconductor Laser Conference (ISLC)* (2010), p. 111.

[82] S. J. Sweeney, Z. Batool, K. Hild, S. R. Jin, and T. J. C. Hosea, in *13th International Conference on Transparent Optical Networks (ICTON)* (2011), p. 1.

[83] E. P. O'Reilly and A. R. Adams, Band-structure engineering in strained semiconductor lasers, IEEE J. Quantum Electron **30**, 366 (1994).

[84] T. Wilson, A. Mellor, N. P. Hylton, and N. J. Ekins-Daukes, in *Proceedings of the 33rd European Photovoltaic Solar Energy Conference and Exhibition* (2017), p. 1257.

[85] G. Luo, S. Yang, J. Li, M. Arjmand, I. Szlufarska, A. S. Brown, T. F. Keuch, and D. Morgan, First-principles studies on molecular beam epitaxy growth of $GaAs_{1-x}Bi_x$, Phys. Rev. B **92**, 035415 (2015).

[86] G. Luo, S. Yang, G. R. Jenness, Z. Song, T. F. Kuech, and D. Morgan, Understanding and reducing deleterious defects in the metastable alloy GaAsBi, NPG Asia Materials **9**, e345 (2017).

[87] S. Mazzucato, P. Boonpeng, H. Carrère, D. Lagarde, A. Arnoult, G. Lacoste, T. Zhang, A. Balocchi, T. Amand, X. Marie, and C. Fontaine, Reduction of defect density by rapid thermal annealing in GaAsBi studied by time-resolved photoluminescence, Semicond. Sci. Technol. **28**, 022001 (2013).

[88] H. Makhloufi, P. Boonpeng, S. Mazzucato, J. Nicolai, A. Arnoult, T. Hungria, G. Lacoste, C. Gatel, A. Ponchet, H. Carrère, X. Marie, and C. Fontaine, Molecular beam epitaxy and properties of GaAsBi/GaAs quantum wells grown by molecular beam epitaxy: Effect of thermal annealing, Nanoscale Res. Lett. **9**, 123 (2014).

[89] V. Sabnit, H. Yuen, and M. Wiemer, High-efficiency multijunction solar cells employing dilute nitrides, AIP Conf. Proc. **14**, 1477 (2012).

[90] R. A. Simmons, S. R. Jin, S. J. Sweeney, and S. K. Clowes, Enhancement of Rashba interaction in GaAs/AlGaAs quantum wells due to incorporation of bismuth, Appl. Phys. Lett. **107**, 142401 (2015).

[91] S. Mazzucato, T. T. Zhang, H. Carrère, D. Lagarde, P. Boonpeng, A. Arnoult, G. Lacoste, A. Balocchi, T. Amand, C. Fontaine, and X. Marie, Electron spin dynamics and g-factor in GaAsBi, Appl. Phys. Lett. **102**, 252107 (2013).